EXPERIMENTAL STUDY OF THE BENDING PERFORMANCE OF HOLLOW GLULAM BEAMS

Peng Shang†
Doctor Graduate Student
E-mail: sp-28@njfu.edu.cn

*Youfu Sun**
Professor
E-mail: yfsun@njfu.edu.cn

Dingguo Zhou†
Professor
Materials Science and Engineering College
Nanjing Forestry University
Nanjing, China
E-mail: dgzhou@njfu.edu.cn

Kai Qin
Graduate Student
Civil Engineering College
Nanjing Tech University
Nanjing, China
E-mail: losco@njtech.edu.cn

Xiaolin Yang
Graduate Student
Architecture College
Zhengzhou University
Zhengzhou, China
E-mail: 124971755@qq.com

(Received January 2017)

Abstract. Hollow glulam beam has some advantages that the traditional solid glulam beam does not have, such as the convenience for wiring construction and comparably light weight. Four-point bending tests of three solid glulam beams and 15 hollow glulam beams with various sizes of rectangular holes produced from small-diameter larch timber were conducted to investigate the influence of the hollow ratio and wall thickness on bending stiffness and load capacity. The midspan deflection, cross-section strain, and ultimate load were obtained from the tests, and the detailed failure modes and apparent MOE for all specimens are reported. Hollow glulam beams with the hollow ratio ranged from 25% to 40%, and the wall thickness greater than 20 mm after the assumption of plane section under bending moment. The apparent bending stiffness and ductility of hollow glulam beam were less than those of solid glulam beam, and the apparent MOE is 0.86 times the elastic modulus value calculated by theory of elasticity. In addition, a calculation formula for the ultimate bending moment is proposed.

Keywords: Hollow glulam beam, bending performance, hollow ratio, wall thickness, ultimate load, deflection.

* Corresponding author
† SWST member

INTRODUCTION

Glulam is a type of high-quality building material and has a lot of advantages such as strength-to-weight ratio, environmental friendliness, and attractive appearance. Glulam materials are applied in the engineering field, which are helpful to reduce the dependence on heavy polluting products, such as steel and cement. Thorough processing can shape glulam into different spans and section sizes to accommodate the wide range of applications (Lestari et al 2015). In addition, the effective use of glulam material consisting of small-diameter lumber, and it is an important approach to the efficient use of wood resources. Under bending, the solid glulam beam exhibits low strain and stress efficiency near the neutral axis. Therefore, the material properties were not fully used. This study proposes a type of glulam beam with a hollow cross section that can realize further optimizations to solid beam. Compared with solid wooden beam, the hollow glulam beam has lighter weight and higher strength-to-weight ratio. The internal hole in the hollow glulam beam can be used to install pipes and cables.

Currently, studies on wooden hollow beam are relatively uncommon. Sasaki conducted a series of studies on the manufacturing technology of hollow cylindrical laminated veneer lumber (LVL) and developed an engineered wood member that consists of a spirally wound LVL encapsulated by a circular steel tube. This hollow cylindrical LVL exhibits high strength and can be used in construction (Sasaki et al 1994, 1996). In addition, Yang and Berard published results on the residual stress distribution and end strength of cylindrical LVL (Yang et al 1999; Berard et al 2011). Studies of hollow cylindrical LVL have mainly focused on processing technology and the mechanical properties needed for column members. Harries conducted axial and flexural tests on hollow built-up columns. All column sections were fabricated from 33 mm sawn timbers glued together. The results are compared with standard calculations of allowable design capacities for nonbuilt-up timber columns. The results show a significant advantage in load-carrying capacity of the built-up sections over solid sections for columns having dimensions greater than 127 × 127 mm. It showed that the ultimate load-carrying capacity of axially loaded specimens is 1.7 times higher than the National Design Specification (NDS) estimates, and the flexural capacity is 3.7 times higher than the NDS estimates (Harries et al 2000). Guo proposed a composite hollow oriented strand board (OSB)-bamboo beam with box section with glue-laminated bamboo as flange and OSB as web. A four-point bending test was conducted on the mechanical properties of 12 beams using parameters such as shear-span ratios and stiffening ribs of composite beams. The results show that when the shear-span ratio is less than 2.0, the composite beam has obvious shear failure characteristics, and the ultimate capacity decreases obviously with the increase in shear-span ratio (Guo et al 2015). Pangfeng (2011) performed tensile, compressive, and bending tests on specimens of laminated larch composite, studied about glued laminated techniques, and processes small-diameter *Larix gmelinii* Rupr plantation, and observed at the effect of diameter of early or late wood on the strength. The results indicated that there were variations in wood properties within and between individual trees. However, the properties of small-diameter *L. gmelinii* Rupr are suitable for its materials as structural glulam. Patterson produced inside-out (ISO) beams with center hole from small-diameter hardwood logs. The test result found that there was no statistically significant difference between the ISO beams and the solid beams in mechanical properties (Patterson and Xiaoling 1998). Hongdi studied the craft and performance of a small-diameter larch and confirmed that the mechanical properties of a beam that consists of small-diameter larch meet the criteria for architectural structures (Hongdi et al 2008). Some researchers have studied the effect of changing the cross sections of beams used in traditional buildings on their bending capacities. Qian adopted a mechanical analysis method to determine the bending capacity of superposed beams and composite beams in historical buildings. The results concluded that the bending capacity of superposed beams with "I-shaped" cross section rarely change compared

with that of beams with the corresponding equal rectangular cross section (Qian and Weiming 2012). Qing performed tests to determine the failure mechanism, the bending capacity, and the strain distribution of superposed timber beams with small tops and large bottoms (Qing et al 2014).

This study tested the bending performance of hollow glulam beams made from small-diameter larch materials and investigated the hollow ratio, wall thickness, and other parameters that influence the bending stiffness and ultimate loading capacity. The study also investigated the failure mechanism, the value of hollow ratio range, and the characteristic MOE for hollow glulam beams.

MATERIALS AND METHODS

Materials

Larch is an important fast-growing tree species and is widely used in China. The excellent mechanical properties of larch can meet the production requirements of glulam (Junling et al 2008). Therefore, fast-growing, small-diameter Xingan larch (*Larix dahurica*) timber was used as the raw material for the hollow glulam beam specimens. The diameters of the larch logs ranged from 100-140 mm, and the ages ranged from 25 to 29 yr. Visual stress grading method was used to select components. According to CNS (2005), the grade of larch logs was II_a. The properties of the materials can be obtained via testing by referring to ASTM (2013). The final MC was 12.84%, and the density was 0.63 g/cm^3. The compressive strength parallel to grain was 43.72 MPa, the tensile strength parallel to grain was 72.58 MPa, and elastic module was 144.15 GPa.

Specimen Design

The hollow glulam beams were processed in Jiangshi Wood Industry Co., Ltd. (Yangzhou, China) at an ambient temperature of 25°C and humidity of 60%. The larch logs were placed into a drying kiln and processed to ensure that the MC was 12%. Then, the raw materials were subjected to sawing, planing, finger jointing, cold-press gluing, and other processing steps. Polyurethane glue was spread at a quantity of 0.2 kg/m^2 by adopting double-sided glue. The laminated splicing pressure was 2.0 MPa over 6 h. The slope of finger joint was 1/10, and the finger length was 20 mm. The finger joints were prevented from appearing in the middle of the two loading point areas of the beam. According to CNS (2005), the grade of lamination was II_b. After gluing, the laminations were glued into the hollow glulam beam with rectangular cross section.

Six groups of specimens, including three solid glulam beams and 15 hollow glulam beams, were constructed with the same length of 3650 mm (fiber direction). All specimens were designed with the same external cross section (100 × 200 mm) and span (3450 mm), with various sizes of internal rectangular holes (50 × 100, 50 × 130, 50 × 160, 40 × 130, and 60 × 130 mm), to determine whether there was any cross-section effect on hollow ratio and wall thickness. The specimen dimensions were designed in accordance with theprocess referenced in ASTM (2015); the cross-section hollow ratio was designed according to CECS (2012). Each group consisted of three identical specimens. The internal hole matched the centroid hole of the external cross section to allow for construction convenience. The hollow ratio of the cross section of the glulam beam can be defined as follows:

$$\varphi = \frac{A}{A_0} \tag{1}$$

where φ is the hollow ratio (%), A is the hollow area of the cross section (mm^2), and A_0 is the gross area of the cross section (including the hollow area, mm^2).

The sectional structure and the schematic diagram of the specimens are shown in Fig 1, where h is the external height of the cross section, b is the external width, h_1 is the internal height, b_1 is the internal width, t_1 is the wall thickness in the height direction, and t_2 is the wall thickness in the width direction. The parameters of the beam specimens and the corresponding values for the

Figure 1. Hollow glulam beam.

cross section are shown in Fig 2 and Table 1. In Table 1, group JHL1 was solid glulam beams and others were hollow glulam beams.

Experimental Methods

The beams were oriented with the longer side vertical, and the test arrangement is illustrated in Fig 3. The displacement of the two supports and the midspan deflection were measured by two linear variable differential transformers (YHD-50, China), and one laser displacement sensor (KEYENCE IL-300, Japan) was installed under the middle span of the beam. Five strain gauges parallel to the longitudinal direction of the beam were symmetrically installed on the side surface of the middle span, and one strain gauge pasted on each of the bottom face and the top face, as shown in Fig 4. The test was formed using a microcomputer-controlled electro-hydraulic servo testing machine with a capacity of 300 kN and a TDS data acquisition system.

The four-point bending experiment was performed according to ASTM (2015). The total load on the beam was symmetrically and monotonously applied at two points equidistant from the reactions. The load was applied initially through a load control program. Taking specimen JHL4-2 as an example, the load was ramped up linearly to 16 kN at a rate of 6 kN/min and then reduced to 4 kN at the same rate. The load was then cycled linearly between 4 and 16 kN, a total of five times to evaluate the elastic modulus accurately. The load was then increased linearly to 30 kN at the same loading rate after which the testing process was changed to displacement control. The test continued at a displacement rate of 5 mm/min until the specimen had sustained significant damage, at which time the testing was

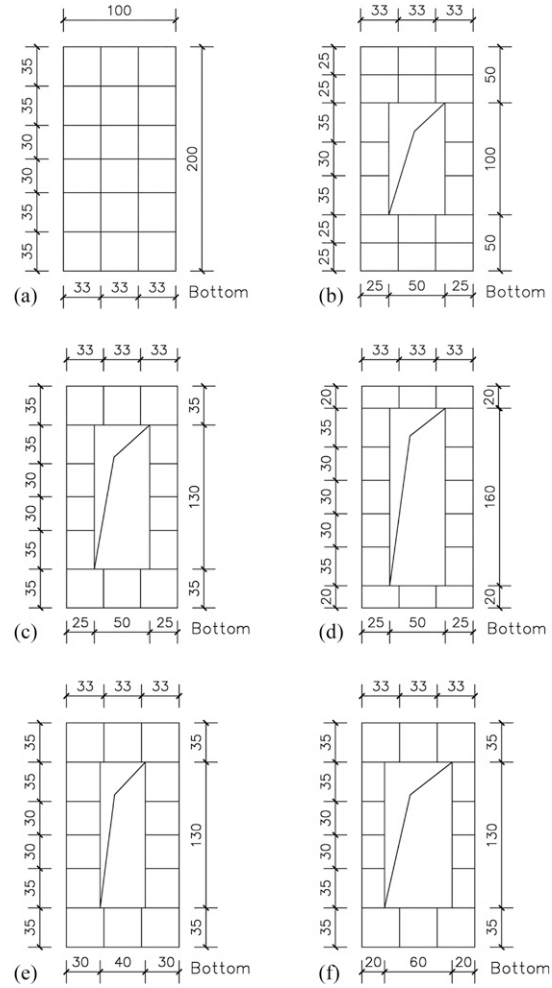

Figure 2. Cross section configuration of the specimens (mm): (a) Group JHL1, (b) Group JHL2, (c) Group JHL3, (d) Group JHL4, (e) Group JHL5, and (f) Group JHL6.

Table 1. Test specimen parameters.

No.	h_1 (mm)	b_1 (mm)	t_1 (mm)	t_2 (mm)	φ (%)
JHL1	–	–	–	–	–
JHL2	100	50	50	25	25.0
JHL3	130	50	35	25	32.5
JHL4	160	50	20	25	40.0
JHE5	130	40	35	30	26.0
JHL6	130	60	35	20	39.0

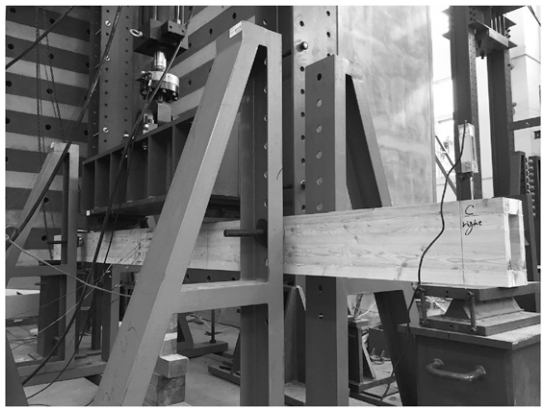

Figure 3. Test site.

halted. The variation of load with time for a typical test is shown in Fig 5.

For bending of the hollow glulam beams, the MOE and the MOR were calculated using Eqs 2 and 3, respectively.

$$\mathrm{MOE} = \frac{a\Delta P}{48I\Delta\omega} 3l^2 - 4a^2 \tag{2}$$

$$\mathrm{MOR} = \frac{P_u a}{2\left(\frac{bh^3 - b_1 h_1{}^3}{6h}\right)} \tag{3}$$

Here, a is the distance between loading support and loading points, ΔP is the load increment in the elastic stage, ω is the deflection of the middle span point under ΔP, l is the span of the beam, I is the moment of inertia of the beam, and P_u is the maximum bending load.

RESULTS AND DISCUSSION

Failure Modes and Mechanism Analysis

Three typical failure modes can be seen from Fig 6. Each specimen behaved elastically at the beginning of loading. Load cycling was undertaken in the elastic region. After completion of cycling, with the increase in loading, 1) the hollow glulam beams (specimens JHL2-3, JHL3-1, JHL3-3, JHL6-1, JHL6-3; groups JHL4 and JHL5) showed a small amount of plastic deformation, and the stiffness of the beams decreased markedly. As the deflection became obvious, cracks

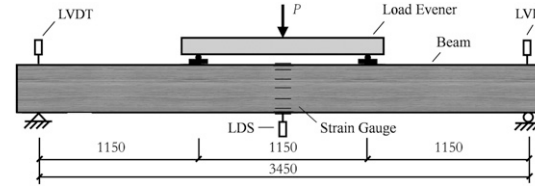

Figure 4. Test setup.

(accompanied by a slight noise) appeared on the bottom tensile surface. Once the bottom-most layer of fibers separated, the beam split longitudinally, and the whole specimen was damaged instantaneously. In these phenomena, the load decreased suddenly as soon as the beam split. The beams shed most of the load at this time and could be considered to have failed. These beams failed at the bottom surface and split up the middle through the height of the beam. The failure of these specimens was characterized by the brittle tensile failure. Figure 6(a) and (b) illustrates this failure mode of the typical specimen JHL5-1. 2) Figure 6(c) and (d) illustrates the second typical failure mechanism of the hollow glulam beams. The bottom fiber of the beam was pulled apart layer by layer gradually, and damage occurred in the midspan area of the beam where there was a larger bending moment. As the outermost layer fiber at the bottom bears the highest tensile stress, the fiber was torn apart layer by layer in the loading process. Different from the first failure

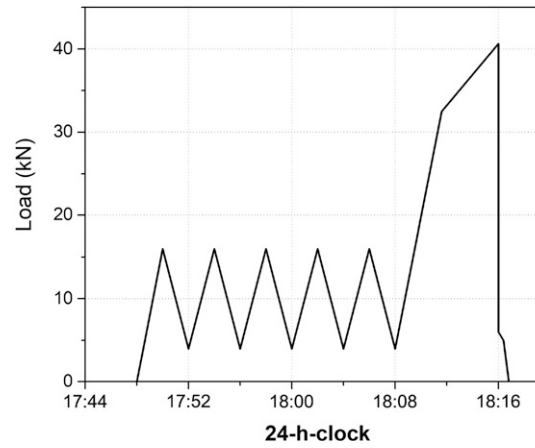

Figure 5. Typical loading regime (specimen JHL4-2).

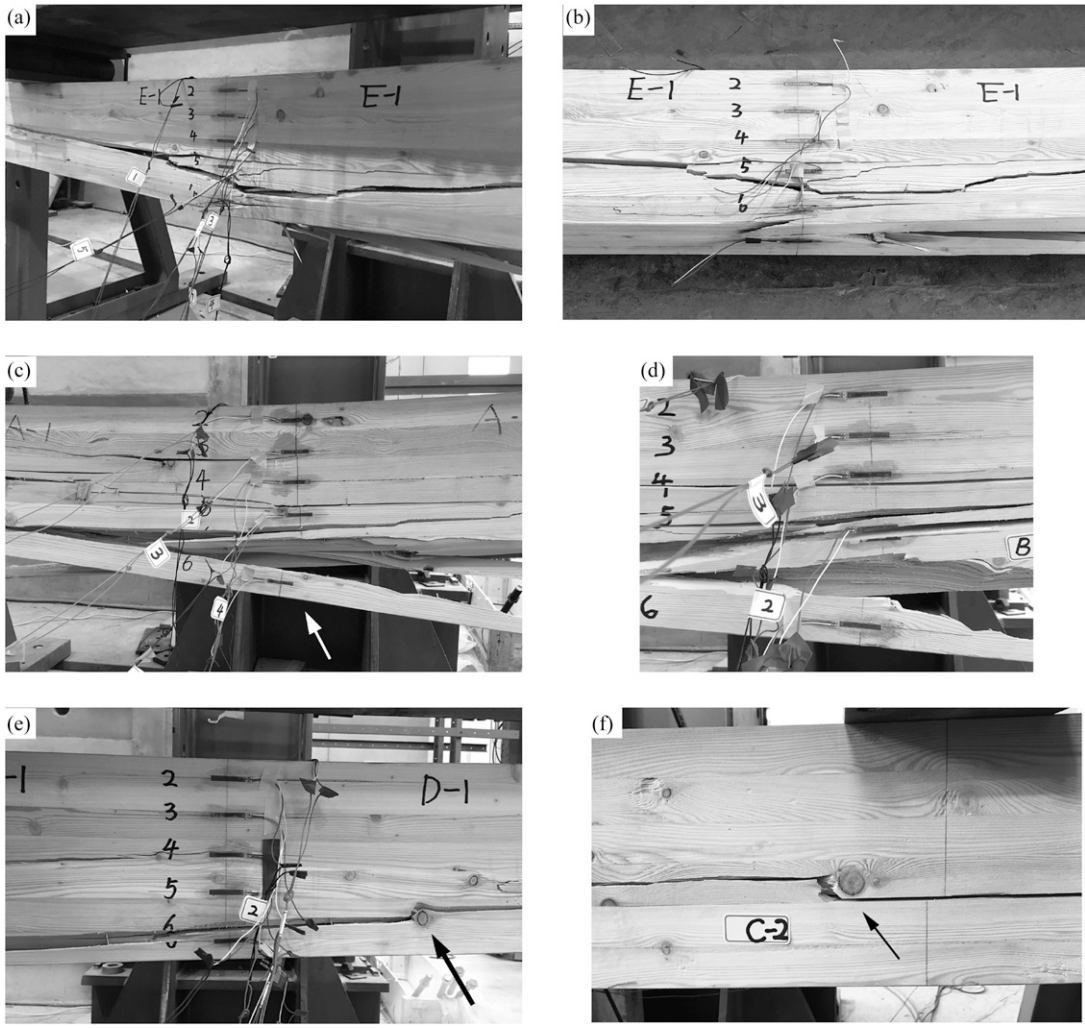

Figure 6. Failure photos of the specimens: (a, b) Typical failure mechanism of the hollow glulam beams, (c, d) Typical failure mechanism of the solid glulam beams and specimen JHL2-3, and (e, f) Knot crack failure mechanism.

mechanism, when the ultimate load was reached, the solid glulam beams (JHL1-1and JHL1-3) and the hollow glulam beam JHL2-3 were not damaged instantaneously. The breakage of fiber proceeded slowly in a cross-saw tooth shape for a while. These specimens were characterized by the gradual tensile failure of the bottom fibers. The failure of specimens has certain ductility. 3) Knot crack failure mechanism (JHL2-1, JHL2-2, JHL3-2, and JHL6-2) occurred when a small amount of inevitable knots remain on the laminations with grade II_b. Knots on the midspan of the beam or near the loading points remarkably affected the bending performance (Fig 6[e] and [f]). The precursor of this failure mode was not obvious. Knots considerably weakened the tensile strength of lumber. Under the load of bending moment, the specimen with knot crack failure mechanism cannot meet the strength requirements.

Experimental Results

The detailed test results for all 18 specimens are presented in Table 2. P_u is the ultimate load, ε_c is

Table 2. Bending test results.

No.	P_u (kN)	ε_c ($\mu\varepsilon$)	ε_t ($\mu\varepsilon$)	ω (mm)	E_{app} (MPa)	MOR (MPa)
JHL1-1	65.56	−4488	3785	62.76	14,075	56.55
JHL1-2	58.37	−3844	5451	49.99	15,043	50.34
JHL1-3	63.52	−3172	5384	62.00	13,495	54.79
JHL2-1	30.98	−2431	2936	33.26	11,670	28.50
JHL2-2	40.29	−2513	2263	35.86	14,380	37.07
JHL2-3	53.28	−4216	3058	53.71	13,585	49.30
JHL3-1	43.82	−2433	4874	80.56	12,930	43.81
JHL3-2	36.31	−1534	2312	49.38	13,018	36.30
JHL3-3	52.66	−4508	5350	67.68	13,018	52.65
JHL4-1	40.31	−6582	3467	70.05	12,218	46.73
JHL4-2	40.63	−8385	4426	54.49	12,720	47.10
JHL4-3	42.97	−3291	4244	69.73	12,730	49.81
JHL5-1	49.45	−4610	3943	58.89	11,301	47.91
JHL5-2	49.83	−3926	3390	56.97	12,781	48.28
JHL5-3	52.51	−4328	3271	56.36	14,115	50.88
JHL6-1	46.62	−5596	3638	69.75	11,170	48.14
JHL6-2	26.82	−1995	1525	35.03	11,943	27.84
JHL6-3	45.01	−3914	3419	48.70	13,412	46.80

the ultimate compressive strain at failure, ε_t is the tensile strain at failure, ω is the deflection of the midspan point, and E_{app} is the apparent MOE. Figure 7 shows the plots of the load against displacement for each group. The five load cycles between 4 and 16 kN showed so little variation that the cycling was not visible in the graph (all cycles plot over the top of the main elastic loading line). For the group JHL1 of solid glulam beams, there was good consistency in the load–displacement response for each of the three specimens. The ultimate load showed a slight difference with the load 58.37-65.56 kN. The load–deflection curves indicated that for the groups JHL1 to JHL6, the falloff of bending stiffness could be divided into three stages. In the first stage, these specimens showed clear elastic behavior up to a load of approximately 70% the ultimate load, followed by nonlinear softening behavior up to the ultimate load, which was the second stage. In this stiffness degradation stage, cracks parallel to grain continuously appeared on the bending surface of the beam and growingly expanded with the increase in load. The slope of the load-deflection curve gradually decreased, whereas the stiffness kept reducing; some plastic characteristics were shown on the solid glulam beams. The third stage was the failure stage. For most specimens, when the load reached the ultimate load, the fibers on the bottom were pulled off. The specimens failed suddenly and shed most of the load. The load decreased suddenly once the beam split. These specimens did not show any ductility behavior before failure, so the failure was relatively brittle in nature. In addition, for the solid beam groups JHL1 and group JHL2 with a greater wall thickness at the bottom, a certain residual loading capacity was maintained after the damage occurred, and with the continual increase in the deflection, the specimens failed suddenly.

Strain Distribution

As the load gradually increased, the midspan deflection and the strain increased. Figure 8 plots the evolution of strain profile through the loading for the midspan cross section of the solid beam JHL1 (Fig 8[a]) and the typical hollow glulam beam JHL3 (Fig 8[b]). P_u is the ultimate load. Each test shows that the strain across the cross section of the hollow glulam beam was basically linear throughout the loading process, following standard beam theory, and the influence of shearing effect on the bending of the beam may be neglected. The envelope of longitudinal strain remained linear; in other words, the strain at each point of the section was proportional to the

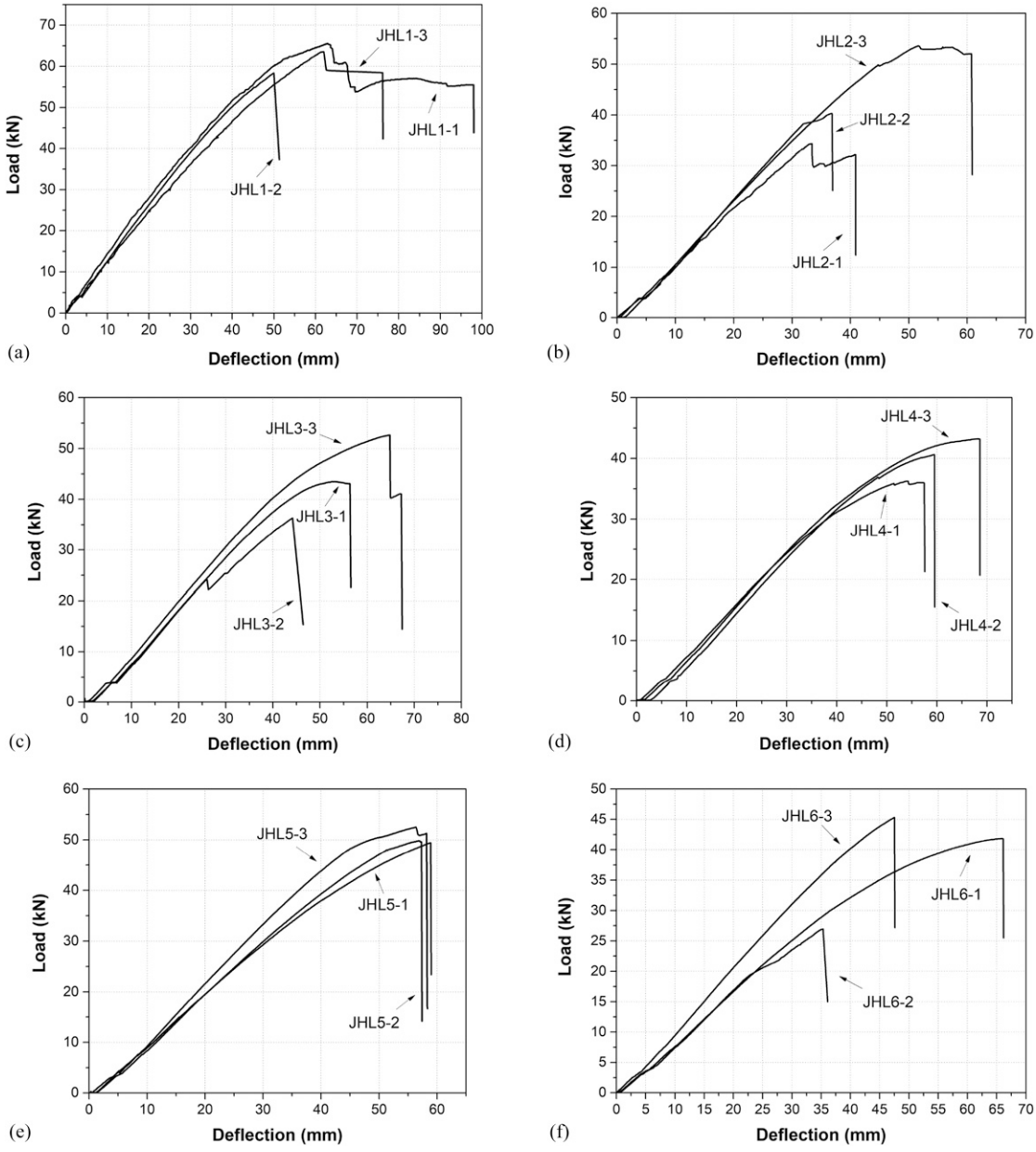

Figure 7. Load–deflection responses.

distance from the neutral axis. With the load increased, the neutral axis gradually moved downward from the center of the beam, particularly during the latter part of the process, which indicated the difference between the tensile behavior and the compressive behavior of lumber. When the specimen lied near failure, the maximum tensile strain of the fiber in the tension area was about 4000 με, and only a small fraction of the specimens had that of 5000 με. The maximum compressive strain of the fiber in the compressive area was about 4500 με, and only

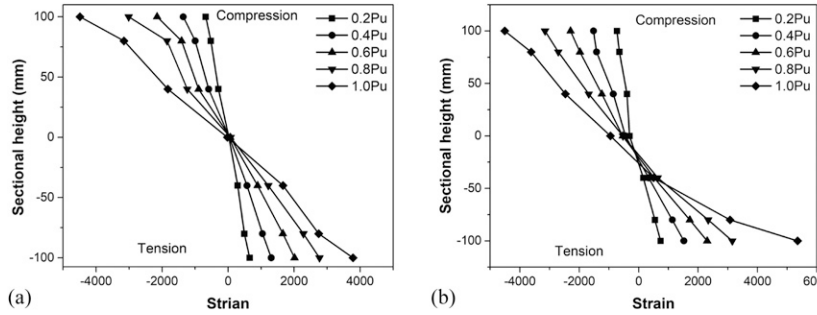

Figure 8. Typical strain profile development for the midspan cross section: (a) Specimen JHL1 and (b) Specimen JHL3.

few of the specimens had that of 5500 με. Once again verifying the conclusion that the fiber in the upper compression area of the section first yielded in the bending process.

Figure 9 plots the load against the top and bottom strain at the midspan cross section for two typical specimens (JHL1 and JHL4). These figures show that the initial elastic moduli for both compression and tension are approximately equal. The compressive strain deviated from the initial elastic slope sooner than the tensile strain, which results from the fact that the tensile strength of the glulam material is greater than its compressive strength, causing the fibers in the compression to first enter the plastic stage.

Figure 10 plots the height of the neutral axis against the load for JHL4 and JHL5. This figure shows that the descent of the neutral axis coincided with the onset of nonlinear deformation observed in the load–displacement diagrams (Fig 7). Almost all other groups of specimens demonstrated the same behavior. When the applied load reached the elastic limit, the fibers in the compression area entered the plastic state gradually and the compression elastic modulus decreased, leading to the internal force redistribution of the cross section. Thus, the neutral axis descended to achieve a new equilibrium.

Bending Stiffness

The statistical values of the bending test results are reported in Table 3. I is the moment of inertia, E is the MOE obtained by material test, and CHAR value stands for characteristic value. Table 3 shows that based on five groups of hollow glulam beams, the mean apparent bending MOE was 12,752 MPa, with a standard deviation of 372 MPa and a coefficient of variation (COV) of 2.92%. Testing the material properties of glulam, the mean bending MOE was 14,415 MPa, with

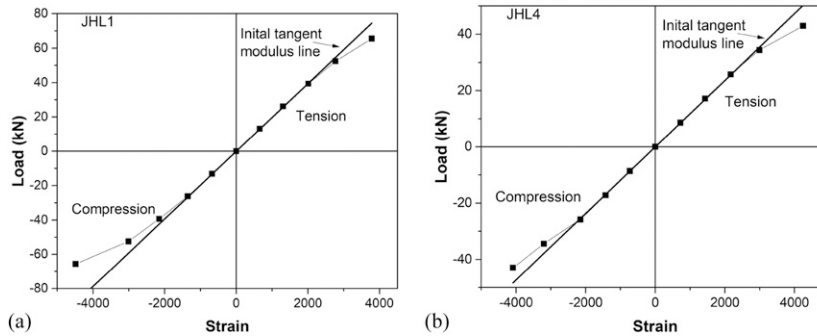

Figure 9. Typical load–strain curves for the midspan cross section: (a) Specimen JHL1 and (b) Specimen JHL4.

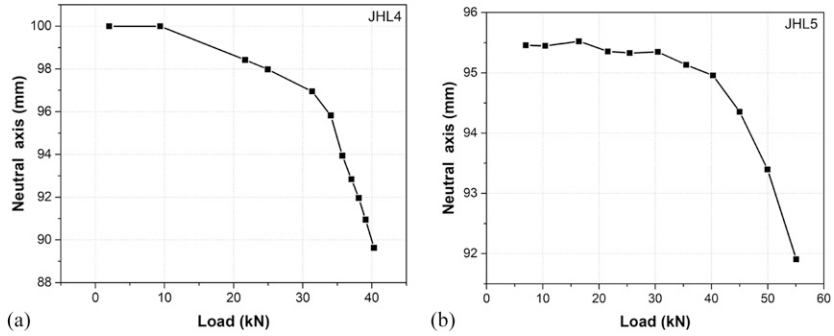

Figure 10. Descent of the neutral axis during the loading process (typical): (a) Specimen JHL4 and (b) Specimen JHL5.

a standard deviation of 218 MPa and a COV of 1.50%. Based on the bending test and referring to CNS (2005), the average deflection at ultimate load of the glulam beam was far bigger than the maximum allowable design value and is 4.5 times the design value. The test value could not meet the requirements of deformation in the code for the design of glulam structures. However, the criterion for hollow glulam beam is normally deflection rather than strength. For structure design, the characteristic elastic modulus is more reliable. Based on the apparent and standard deviation quoted, the characteristic apparent MOE for hollow glulam beams is 12,140 MPa and for glulam material is 14,059 MPa. This is the value expected to be exceeded by 95% of specimens and was calculated using Eq 4,

$$E_k = \mu_f\left(1 - 1.645\delta_f\right) \quad (4)$$

where E_k is the characteristic elastic modulus, μ_f is the average value, and δ_f is the COV.

Table 3 illustrates the comparison between the apparent elastic modulus obtained by bending experiment and the elastic modulus obtained by material test. The apparent bending stiffness of the glulam beams was determined by the product of the cross section moment of inertia and the apparent elastic modulus. The apparent elastic modulus of solid glulam beam is approximately consistent with the elastic modulus obtained by material test. However, the cross sections with holes weakened the elastic modulus of the hollow glulam beams. The apparent bending stiffness of hollow glulam beams is slightly lower than the value calculated by the theory of elasticity and 0.86 times the calculation value when the hollow ratio ranged from 25% to 40%. Therefore, the reduction coefficient should be considered when estimating deformations to the

Table 3. Statistical values of the bending test results.

No.	P_u (kN)	ε_c (με)	ε_t (με)	ω (mm)	I (mm^4)	MOR (MPa)	E_{app} (MPa)	E (MPa)	$\frac{E_{app}}{E}$ (%)
JHL1	62.48	−4488	3785	62.38	6.67×10^7	53.89	14,204	14,325	0.99
JHL2	53.28	−4216	3058	53.71	6.25×10^7	49.30	13,212	14,844	0.89
JHL3	48.24	−4508	5350	74.12	5.75×10^7	48.23	13,084	14,538	0.90
JHL4	41.30	−3291	4244	69.89	4.96×10^7	46.40	12,557	14,269	0.88
JHL5	50.06	−4610	3943	54.71	5.93×10^7	49.02	12,733	14,307	0.89
JHL6	45.82	−5596	3638	59.14	5.57×10^7	43.23	12,175	14,205	0.86
Average[a]		−4452	4003	62.31		47.24	12,752	14,415	
Std dev[b]		676	701	8.23		2.24	372	218	
COV[c] (%)		15.10	17.51	13.21		4.75	2.92	1.50	
CHAR							12,140	14,059	0.86

COV = coefficient of variation.
[a, b, c] The value of apparent MOE was calculated for the hollow glulam beams (JHL2 to JHL6).

hollow glulam beams. In addition, for the specimens (group JHL2, JHL3, and JHL4) with the same wall thickness and internal width, they also have different hollow ratio. While the hollow ratio was 25%, 32.5%, and 40%, respectively, the apparent elastic modulus decreased. Figure 11 plots that the curve almost decreases linearly. For the specimens (group JHL4 and JHL6) with the same hollow ratio and the apparent elastic modulus, the bending stiffness of JHL6 was approximately 11.3% higher than that of JHL4 because of the different moment of inertia.

Figure 12 indicates the relationship between the bending stiffness and the hollow sectional shape varied by the hollow ratio. As mentioned previously, where $E_{app,k}$ is 12,140 MPa and E_k is 14,059 MPa; I_1 is the moment of inertia of the hollow section and I_0 is the moment of inertia of the solid section. Figure 12(a) shows that for cross section with the same hollow ratio, the bending stiffness shows an increase tendency as the internal width b_1 increased. The slope and rate were more obvious with greater hollow ratio and wider internal width. Conversely, Fig 12(b) shows that for specimens with the same hollow ratio, the bending stiffness tends to decrease gradually with the increase in the internal height h_1, and the decrease rate would faster with greater hollow ratio. Consequently, for hollow glulam beam with superimposed centroid and constant hollow ratio, the internal width should be enlarged first to increase the bending stiffness of the section.

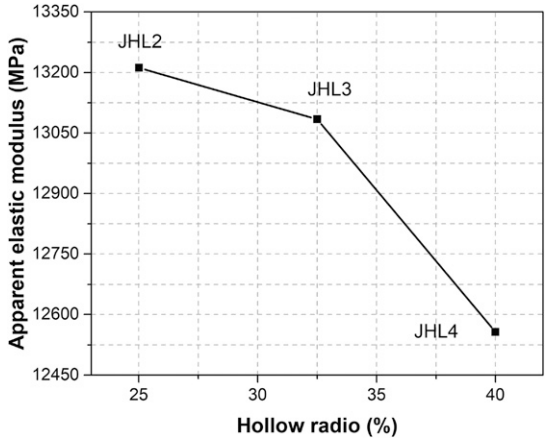

Figure 11. Relationship between the hollow radio and the apparent MOE.

Load Capacity

According to the failure mechanism of each specimen and the data measured in Table 2, in specimens JHL2-1, JHL2-2, JHL3-2, and JHL6-2, initial defects such as knots occur because the specimens become damaged before achieving the estimated ultimate load. The deformation of the tensile and compressive region has not been developed completely. Consequently, the four specimens were removed. The hollow section has a great influence on the plastic deformation of the material, and it also affected the loading capacity. When the load increased, the fiber in the top of the compression area of the beam, which was over the neutral axis of the section, first reached the plastic state, leading to the internal force redistribution of the cross section. Subsequently, the damage occurred on the beam bottom when the fiber of the tensile area reached the ultimate tensile stress. Figure 7 shows that JHL1 reached the elastic-plastic state when the load reached about 50 kN. With the rapid increase in deflection and strain, the ultimate load reached 62 kN, and the load increased in the elastic–plastic state about 19.4% of the ultimate load. However, the hollow glulam beams did not show an obvious yield deformation stage compared with the solid glulam beam, the development of plastic deformation was smaller, and the ultimate load decreased in large amplitude. Table 3 shows that for the hollow glulam beams, the cross-section area decreased by 25%, 26%, 32.5%, 39%, and 40% compared with the solid glulam beam, whereas the ultimate load decreased in the hollow glulam beams were 14.7%, 19.9%, 22.8%, 26.7%, and 33.9% of the ultimate load of JHL1. Figure 13 shows that for specimens with the same internal width (JHL2, JHL3, and JHL4) or internal height (JHL5, JHL3, and JHL6), the ultimate load decreased with the increase in the hollow ratio, and the curve decreased linearly.

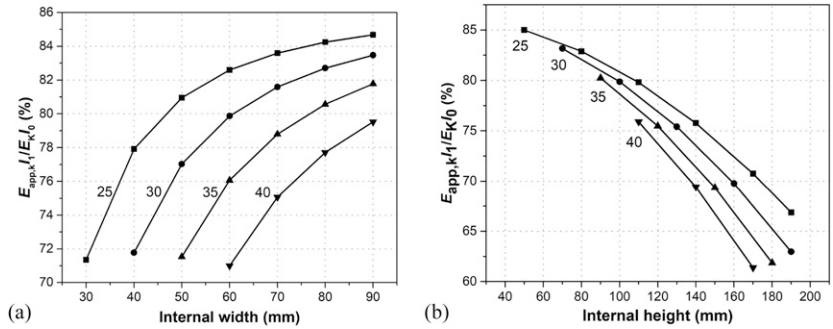

Figure 12. Relationship between the section shape and the bending stiffness: bending stiffness with the same hollow ratio and (a) variable internal width and (b) variable internal height.

The average deflection at the ultimate load of the hollow glulam beams was 62.3 mm, which was far greater than the maximum allowable design value of 13.8 mm. The serviceability limit state design specified in the Chinese wood structure design specification CNS (2005) states that the middle deflection should be less than $l/250$ (where l is the span of the beam). The average deflection at the ultimate load of hollow glulam beams is 4.5 times the design value, and the maximum ultimate deflection of the hollow beams can reach $l/47$ before damage. However, the critical design criterion for hollow glulam structures is generally deflection rather than strength. In addition, the advantage of deflection over strength is that it can be measured directly on the beam. Consequently, hollow glulam beams with various hollow ratios (JHL2 to JHL6) have a certain surplus of strength.

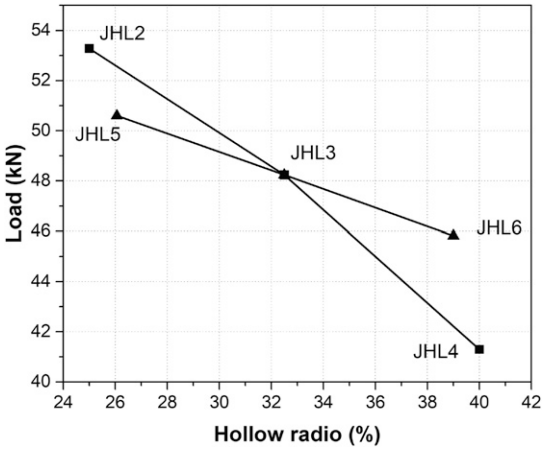

Figure 13. Relationship between the ultimate load and the hollow radio.

Deformation Calculation

The apparent bending stiffness of the hollow glulam beams is slightly smaller than the value calculated using the theory of elasticity. The hollow glulam beam structurally designed by the theory of elasticity, the calculated deflection may be smaller than the actual value, which is unsafe for structure designs. Therefore, a reduction coefficient γ was added to reduce the bending stiffness calculated using the theory of elasticity. Hence, the effective apparent bending stiffness of the hollow glulam beam can be expressed as follows:

$$E_{\mathrm{app,k}}I = \gamma E_{\mathrm{k}}I \tag{5}$$

where $E_{\mathrm{app,k}}$ is the effective bending stiffness of the glulam beam (N/mm^2), E_{k} is the elastic modulus obtained by material test (N/mm^2), I is the moment of inertia (mm^4), and γ is the reduction coefficient, which is 0.86 for the hollow glulam beam.

Considering the bending test results for the hollow glulam beam and based on the static equation, the midspan deflection of the beam can be expressed as follows:

$$\omega = \frac{Pa}{48E_{\mathrm{app,k}}I}\left(3l^2 - 4a^2\right) \tag{6}$$

where ω is the deflection of the midspan point under P (N/mm^2), P is the concentrated load on

the glulam beam (N), l is the span of the beam (mm), a is the distance between the loading support and loading points (mm), and $E_{app,k}I$ can be obtained from Eq 5 ($N \cdot mm^2$).

Figure 14 plots the load against deflection for the glulam beams, respectively. The comparison between the calculated deflection obtained from Eq 6 and the experimental deflection of each specimen shows that the calculated values were generally consistent with the experimental values. Both the curves in the elastic state were less than that of experimental curves, which indicated that a certain redundancy was reserved for the hollow glulam structural design. Consequently, the method to calculate the deflection of hollow glulam beams is feasible.

Ultimate Loading Capacity Calculation

Li (2011) proposed a calculation method of the bending capacity of the solid glulam beam. The method assumed that the mean strain of the cross section was in accord with the plane-section assumption and adopted the constitutive relationship for laminated wood suggested by Chen (2003). As shown in Fig 15, the material would be regarded as an elastic perfectly plastic material under compression, and it would be regarded as a perfectly elastic material under tension. Hence, the analytical expressions of the stress–strain model can be given as follows.

$$\sigma_c = \begin{cases} E\varepsilon_c, & 0 \le \varepsilon_c \le \varepsilon_{ce} \\ f_{ce}, & \varepsilon_{ce} \le \varepsilon_c \le \varepsilon_{cu} \end{cases} \tag{7}$$

$$\sigma_t = E\varepsilon_t, \quad \varepsilon_t \le \varepsilon_{te} \tag{8}$$

where σ_c is the compression stress value of the fiber in the compression area (MPa), ε_c is the compression strain value ($\mu\varepsilon$), ε_{ce} is the ultimate elastic compression strain ($\mu\varepsilon$), f_{ce} is the stress value when the fiber reached the ultimate elastic compression strain (MPa), ε_{cu} is the ultimate compression strain value ($\mu\varepsilon$), σ_t is the tensile stress value (MPa), ε_t is the tension strain value ($\mu\varepsilon$), ε_{te} is the ultimate elastic tensile strain value ($\mu\varepsilon$), and f_{te} is the stress value when the fiber reached the ultimate elastic tensile strain (MPa).

For the solid glulam beam, the fiber at the bottom reached the ultimate strain under the ultimate bending moment, which shows that the fiber in the compression area reached the plastic stage synchronously. According to the constitutive relationship of Chen (2003) and the assumption of the failure mechanism, the section can be subdivided into three areas based on the height. The top area is the plastic compression area; the area between the plastic area and the neutral axis is the elastic compression area; and the area under the neutral axis is the tensile area. Therefore, the diagrams of the stress and strain over the section can be plotted as shown in Fig 16.

In this figure, αh is the height of the plastic compression area, βh is the height of the elastic compression zone, and γh is the height of the elastic tensile zone. If $f_{te}/f_{ce} = n_0$ and $\gamma h/\beta h = n_0$, then the material test indicates that $n_0 \approx 2$. Based on the static equilibrium of the section, the height of the neutral axis and the ultimate bending moment of the solid glulam beam can be obtained by the following equation:

$$\xi = \alpha h + \beta h = \frac{n_0^2 + 1}{(n_0 + 1)^2} \cdot h \tag{9}$$

$$M_{u,0} = \frac{3n_0 - 1}{6(n_0 + 1)} f_{ce} b h^2 \tag{10}$$

where ξ is the height of the neutral axis (mm) and $M_{u,0}$ is the ultimate bending moment of the solid glulam beam ($kN \cdot m$).

For normally designed hollow glulam beams (group JHL2 to JHL6), the fiber on the bottom of the beam reached the ultimate strain under the ultimate bending moment, which is a sign of damage. Therefore, the diagrams of the stress and strain over the hollow glulam beam section under the ultimate bending moment can be plotted as shown in Fig 17.

According to the test results, for the hollow glulam beam, the height of the plastic compression area was greater than the wall thickness t_1 in the height direction. As the hollow glulam beam section changed in the width direction, the resultant force of the plastic compression area can

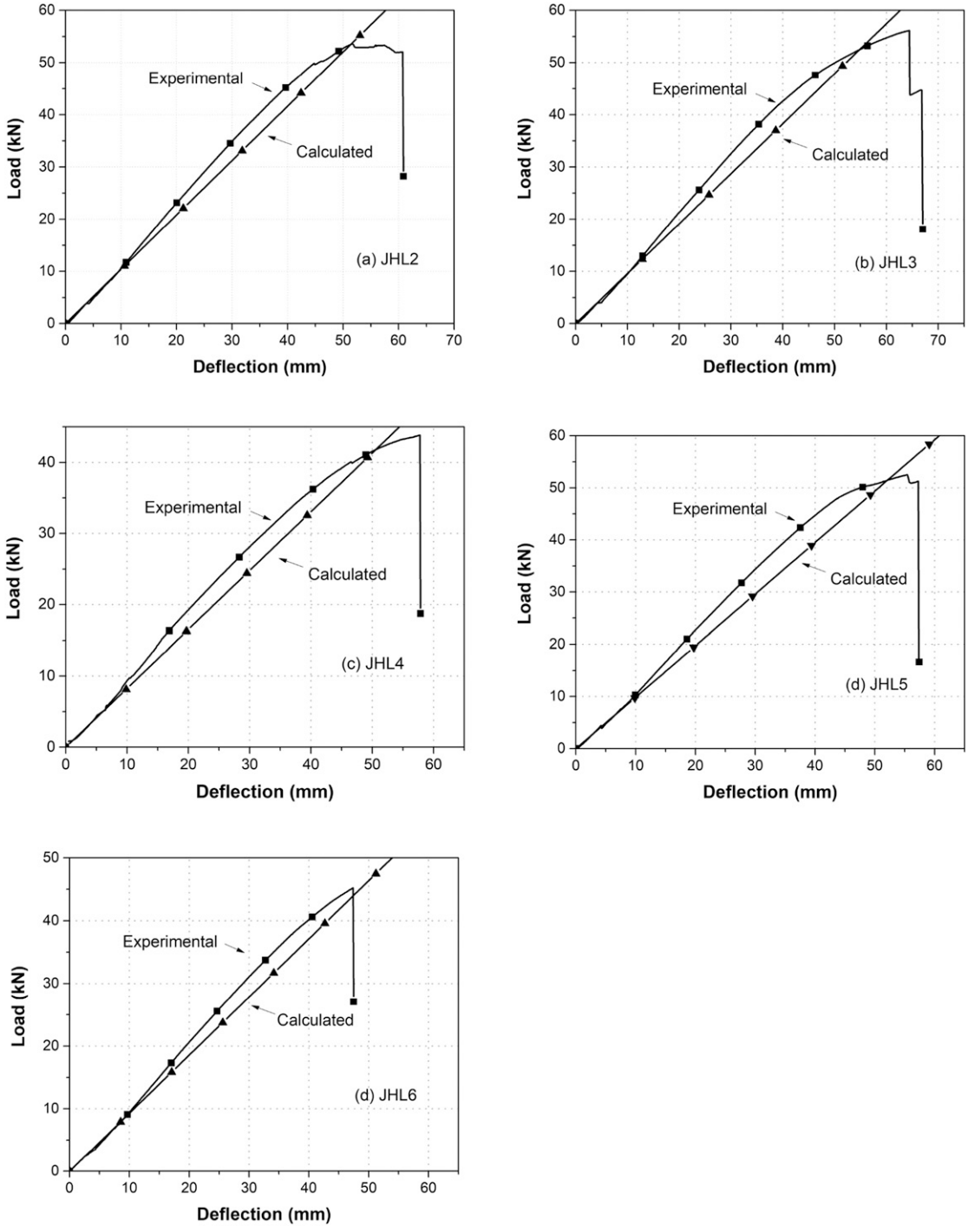

Figure 14. Comparison between the calculation and experimental deflection results.

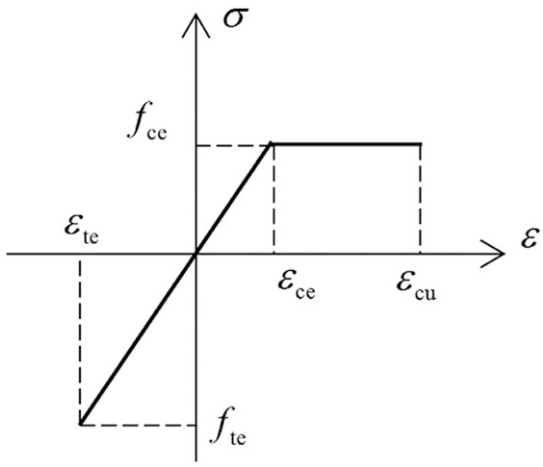

Figure 15. Strain–stress curve.

be subdivided into F_{cp1} and F_{cp2}, and the resultant force of the elastic tension area subdivided into F_{te1} and F_{te2}. For the hollow glulam beam, the ultimate tension strain value is associated with the internal height h_1 of the section. Therefore, the specific value of f_{te} and f_{ce} can be expressed as follows:

$$n = \frac{f_{te}}{f_{ce}} = 2 - \left(\frac{h_1}{h}\right)^{1.3} \tag{11}$$

where n is the specific value of f_{te} and f_{ce} of the hollow glulam beam.

According to the balance of the axial force, the force moment was obtained by taking the subdivided force against the neutral axis. The height coefficient of each area of the section α, β, and γ, and the ultimate bending moment M_u of the hollow glulam beam can be obtained for the ultimate limit state. These values can be calculated as follows:

$$\beta = \frac{\psi + \sqrt{\psi^2 + 2(b-2t_2)(n+1)^2 t_1^2 t_2 h^2}}{2(n+1)^2 t_2 h^2} \tag{12}$$

$$\psi = (2t_1 t_2 - bt_1)(n-1)h - 2t_2 h^2 \tag{13}$$

$$\gamma = n \cdot \beta \tag{11}$$

$$\alpha = 1 - \gamma - \beta \tag{12}$$

$$\begin{aligned} M_u = {} & bt_1[(1-\gamma)h - 0.5t_1]f_c \\ & + 2t_2(\alpha h - t_1)[(1-\gamma)h - 0.5(\alpha h + t_1)]f_c \\ & + \frac{2}{3}\left[t_2\beta^2 h^2 + t_2\left(n - \frac{t_1}{\beta h}\right)(\gamma h - t_1)^2\right]f_c \\ & + \frac{bt_1}{2}\left(2n - \frac{t_1}{\beta h}\right)(\gamma h - 0.5t_1)f_c \end{aligned} \tag{14}$$

where M_u is the ultimate bending moment of the hollow glulam beam (kN·m).

To validate the analytical model proposed previously, the ultimate bending moment of the solid glulam beam and hollow glulam beam can be calculated from Eqs 10 and 14. The calculation results which are shown in Table 4 were compared with the experimental results, ξ_c is the

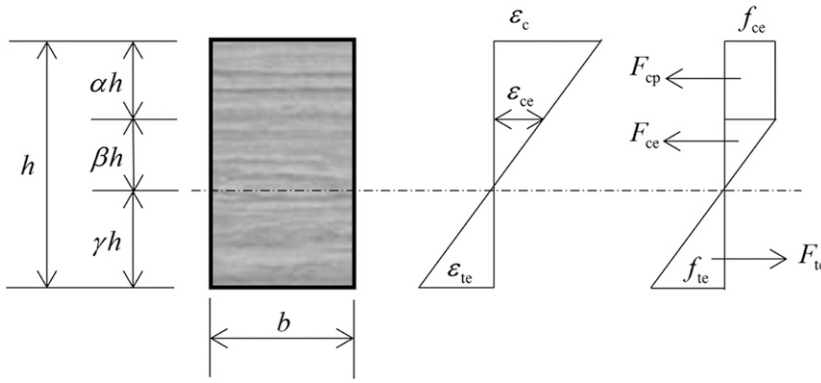

Figure 16. Strain–stress distribution at the ultimate failure state of the solid glulam beam.

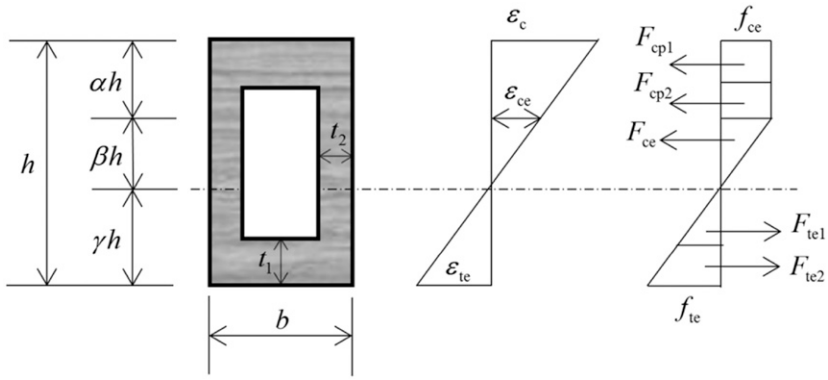

Figure 17. Strain–stress distribution at the ultimate failure state of the hollow glulam beam.

calculation height of the neutral axis; ξ_{exp} is the experimental height of the neutral axis; $M_{u,c}$ is the calculated ultimate bending moment; and $M_{u,exp}$ is the experimental ultimate bending moment. For hollow glulam beams with the hollow ratio ranging from 25% to 40% and wall thickness greater than 20 mm (JHL2 to JHL6), the experimental and calculation results are approximately consistent, which indicated that the method presented in this article for analyzing the bending performance of hollow glulam beams is feasible.

CONCLUSIONS

To investigate the bending performance of the hollow glulam beams, three solid glulam beams and 15 hollow glulam beams were tested. Based on the the analysis of the test data, the following conclusions can be drawn.

1. Three failure mechanisms were observed about the hollow glulam beams, which were characterized by brittle tensile failure initiated at the tension face of the beam. The load-deflection curves are approximately linear, and the strain distribution across the cross section remains approximately linear throughout the loading process, following standard beam theory.
2. The average midspan deflection at the ultimate load of the hollow glulam beams was 62.3 mm, which was far greater than the maximum allowable design value of 13.8 mm. The maximum ultimate deflection can reach $l/47$ before damage. Consequently, the critical design criterion for hollow glulam structures is deflection rather than strength.
3. The cross-section hole weakens the apparent elastic modulus and apparent bending stiffness of the hollow glulam beams. The apparent bending stiffness is slightly smaller than the calculation value by the theory of elasticity and 0.86 times the calculated value. The internal height of the section has a great impact on the ultimate loading capacity and the bending stiffness. The characteristic apparent MOE is 12,140 MPa when the hollow section ranges from 25% to 40% and the wall thickness is greater than 20 mm.
4. The deformation and load capacity of the hollow glulam beam can be calculated by using the theory of elasticity. Based on the test results

Table 4. Comparison between the calculated and experimental values.

No.	ξ_c (mm)	ξ_{exp} (mm)	Error (%)	$M_{u,c}$ (kN·m)	$M_{u,exp}$ (kN·m)	Error (%)
JHL2	89.01	91.08	2.33	32.02	31.97	0.15
JHL3	88.17	87.31	0.97	29.60	28.95	2.27
JHL4	89.19	83.42	6.47	26.06	24.78	5.18
JHL5	89.94	91.90	2.11	30.72	30.36	1.19
JHL6	85.64	80.50	6.00	28.66	27.49	4.23

and analysis, a reduction coefficient should be added to calculate the bending stiffness. A calculation model for the ultimate bending moment was proposed, and the calculation values were consistent with the experimental values. The result shows that the calculation model proposed herein is feasible.

ACKNOWLEDGMENTS

The authors are grateful for the support of the Forestry Industry Research Special Funds for Public Welfare Projects, Grant No. 011020009, and the National Key Technology Research and Development Program, Construction technique upgrading and applying demonstration of the traditional rural house, Grant No. 2015BAL03B03.

REFERENCES

ASTM (2013) D 4761-13. Standard test methods for mechanical properties of lumber and wood-base structural material. American Society for Testing and Materials, West Conshohocken, PA.

ASTM (2015) D 198-15. Standard test methods of static tests of lumber in structural sizes. American Society for Testing and Materials, West Conshohocken, PA.

Berard P, Yang P, Yamauchi H, Umemura K, Kawai S (2011) Modeling of a cylindrical laminated veneer lumber I: Mechanical properties of hinoki (*Chamaecyparis obtusa*) and the reliability of a nonlinear finite elements model of a four-point bending test. J Wood Sci 57(2): 100-106.

CECS (2012) CECS 254-12. Technical specification of hollow concrete-filled steel tubular structures. China Association for Engineering Construction Standardization, Beijing, China.

Chen Y (2003) Flexural analysis and design of timber strengthened with high strength composites. PhD thesis, Rutgers the State University of New Jersey, New Brunswick, NJ.

CNS (2005) GB 50005-03. Code for design of timber structures. Ministry of Housing and Urban Rural Development of the People's Republic of China Press, Beijing, China.

Guo C, Qisheng Z, Dongsheng H, Haitao L, Tao Z (2015) Experimental study on mechanical properties of composite OSB-bamboo beam with box section. Building Structure 45(22):102-106.

Harries KA, Petrou MF, Brooks G (2000) Structural characterization of built-up timber columns. J Archit Eng 6(2): 58-65.

Hongdi W, Jiabin Z, Jincun H (2008) Trial research on plantation small diameter larch compositive beam. Forest Mach Woodwork Equip 36(1):17-20.

Junling W, Hongxi J, Zhanbiao Y, Gang W (2008) Species diversity and productivity of *Larix principis-rupprechtii* plantation woods in Liupan mountains. J Lanzhou University 44(1):31-42 (Natural Sciences).

Lestari ASRD, Hadi YS, Hermawan D, Santoso A (2015) Glulam properties of fast-growing species using ahogany tannin adhesive. BioRes 10(4):7419-7433.

Li Z (2011) Study on the mechanical behavior of timber beams strengthened with carbon fiber reinforced plastics. PhD Thesis, Nanjing Forestry University, Nanjing, China. 32 pages.

Pangfeng Y (2011) Study on glued laminated techniques and processed of small-diameter *Larix gmelinii* Rupr plantation in polygonal cutting. PhD thesis, Northeast forestry university, Harbin, China. 65 pages.

Patterson DW, XiaoLing X (1998) Inside-out beams from small-diameter Appalachian hardwood logs. Forest Prod J 48(1):76-80.

Qian Z, Weiming Y (2012) Bending analysis on composite beam and combination beam of Chinese ancient wooden buildings. Building Structure 42(4):157-161.

Qing C, Chunchao C, Jianwu P (2014) Experimental study on bending behavior of Chinese traditional timber stitching beams with big top and small bottom. J Cent South Univ 45(5):1659-1665 (Science and Technology).

Sasaki H, Kawai S, Ma L (1994) Recent trials on utilization of fast-growing plants. Pages 162-170 *in* International Symposium on the Utilization of Fast Growing Trees, October 15-17, Nanjing, China.

Sasaki H, Yamauchi H, Koizumi A (1996) Cylindrical LVL for structural use made by spiral-winding method. Pages 538-540 *in* International Wood Engineering Conference, October 28-31, New Orleans, LA.

Yang P, Ohsako Y, Yamauchi H, Sasaki H (1999) Numerical analysis of stress distribution along the glueline between cylindrical LVL column and its reinforcement core for end-joints. Pages 65-69 *in* Pacific Timber Engineering Conference, March, Rotorua, New Zealand.